ARTICLE OPEN ACCESS

Effect of Re or W Addition on the Oxidation Behaviour of a Compositionally Complex Ta–Mo–Cr–Ti–Al Alloy in Air at 1000°C

Björn Schäfer[1] | Michael Dürrschnabel[1] | Carsten Schroer[1] | Fabian Lanoy[2] | Emma White[2] | Mathias Galetz[2] | Chongchong Tang[1] | Bronislava Gorr[1]

[1]Institut für Angewandte Materialien, Karlsruher Institut für Technologie (KIT), Karlsruhe, Germany | [2]Dechema-Forschungsinstitut, Frankfurt, Germany

Correspondence: Björn Schäfer (bjoern.schaefer@kit.edu)

Received: 25 November 2025 | **Revised:** 20 March 2026 | **Accepted:** 31 March 2026

Funding: Deutsche Forschungsgemeinschaft, Grant/Award Number: 467750555

Keywords: doping | refractory high entropy alloy | rutile-type complex oxide | thermogravimetry

ABSTRACT

Presuming that doping of protective $(Cr,Ta,Ti)O_2$ with cations of +5 or higher valence further improves the oxidation resistance of Ta–Mo–Cr–Ti–Al, the effect of 3 at.% of Re or W in otherwise equimolar Ta–Mo–Cr–Ti–Al is investigated in oxidation tests performed at 1000°C in air. Both minor additions indeed decrease the parabolic mass gain (72 h), which for W also manifests in reduced thickness of oxide layers and zone of internal corrosion that persists for at least 100 h. Besides the hypothesised doping, other factors that may explain the effect of Re or W are discussed. A general finding of the analytical work is the identification of $(Ti,Ta)O_2$ with Mo inclusions underneath the inward growing $(Cr,Ta,Ti)O_2$ layer.

1 | Introduction

Refractory compositionally complex alloys (RCCA) or high entropy alloys (HEA) in the Ta–Mo–Cr–Ti–Al system are currently receiving attention as a promising basis for the development of materials that retain high strength at 1000°C or well beyond, while outperforming other refractory metal alloys in terms of high-temperature oxidation resistance [1–4]. The trigger for the latter is seen in the establishment of a complex oxide of rutile structure, which primarily contains Cr, Ta and Ti, besides oxygen [1]. The oxide $(Cr,Ta,Ti)O_2$ forms a thin layer in the oxide scale on the surface of Ta–Mo–Cr–Ti–Al alloys, with the ratio of Cr, Ta and Ti cations depending on alloy composition [1]. It features growth rates comparable to the classic protective oxides [3], and as a Ti-free variant, also forms on Ni, Co or Fe alloys [5–7].

To date, oxidation performance in air has been best investigated for the equimolar alloy referred to as TaMoCrTiAl in the following. At 1000°C in air, the complex oxide is capable of forming a continuous layer already after 4.5 h [4] and if formed at 1500°C, does not detach from the substrate alloy even during rapid cooling to room temperature [3]. The atom ratio of the cations in $(Cr,Ta,Ti)O_2$ is roughly 1:1.4:1.4 [1]. Other features of the oxide scale are TiO_2, Al_2O_3 and Cr_2O_3 that presumably have grown outward during the transient stage, and now prevail above the $(Cr,Ta,Ti)O_2$ layer. Underneath the latter, Cr depletion and internal corrosion, notably Al_2O_3 and TiN precipitation, are observed. Dedicated experiments [4] show that the $(Cr,Ta,Ti)O_2$ grows inward, suggesting that mass transport in this oxide is dominated by oxygen diffusion via vacancies in the anion sublattice. In terms of thickness, the zone of internal corrosion tends to grow faster than the $(Cr,Ta,Ti)O_2$ layer. Cation diffusion is regarded as not relevant based on the observation that the outer oxides do not reform after removal from the scale, at the $(Cr,Ta,Ti)O_2$/gas interface [4]. The role attributed to Mo is largely confined to the formation of volatile oxide [4].

It seems rather unlikely to find compositions in the Ta–Mo–Cr–Ti–Al system for which adequate oxidation resistance and

mechanical properties are combined in a single alloy, especially if considering that, additionally, a reduction in mass density of the typically heavy alloys may be requested for certain applications [8]. This may lead to the situation that further, minor addition of elements to the alloys is taken into account, with the intent to improve one property (oxidation resistance or mechanical) without disturbing another (such as mass density). As for oxidation resistance, it is generally accepted that a minor addition to the alloy may measurably affect the performance via doping of a protective oxide, to the better or the worse. The doping essentially consists of this minor element transferring from the alloy into the respective oxide, which alters the concentration of the defects responsible for mass transport through the oxide sublattices [9, 10]. An indicative number for the dopant concentration necessary to effectively influence the defect concentration in oxides has been found for the eponymous rutile TiO_{2-x}, which is the order of 50 ppm by mass [11].

The aim of this study is to investigate if adding a sixth element in a relatively small amount to TaMoCrTiAl takes a beneficial effect on oxidation performance as qualitatively predictable by doping of the protective $(Cr,Ti,Ta)O_2$ layer. The candidates for such addition are Re and W, which according to the defect equilibria

$$9V_O^{\bullet\bullet} + 3Re_2O_7 = 2Re_{Cr}^{\bullet\bullet\bullet\bullet} + 2Re_{Ti}^{\bullet\bullet\bullet} + 2Re_{Ta}^{\bullet\bullet} + 21O_O \quad (1)$$

$$6V_O^{\bullet\bullet} + 6WO_3 = 2W_{Cr}^{\bullet\bullet\bullet} + 2W_{Ti}^{\bullet\bullet} + 2W_{Ta}^{\bullet} + 18O_O \quad (2)$$

should lead to a decrease in the number of oxygen vacancies $V_O^{\bullet\bullet}$ in the complex oxide if incorporated as Re^{7+} or W^{6+} cations. Such decrease in the concentration of $V_O^{\bullet\bullet}$, a determinant of oxygen transport, is generally predicted for foreign cations of valance higher than the average in $(Cr,Ta,Ti)O_2$, that is, +4, and presumably results in decelerated growth in comparison to the undoped oxide. Oxygen vacancies may play a qualitative similar role in nitrogen passing the $(Cr,Ti,Ta)O_2$ layer via the anion sublattice, that is, for internal corrosion carried forward by nitride precipitation. The defect equilibria presented as Equations (1) and (2) assume equal replacement of the principal cations in the oxide, are good for demonstrating the principle, but in practical cases, the change in oxygen vacancy number per foreign cation incorporated will differ. Furthermore, such doping largely alters intragranular diffusion, while transport along oxide grain boundaries may remain unaffected. This and other factors relating to the complexity of the alloy system and oxide scales formed may challenge the predictive power of the doping effect in the case under consideration.

In a first attempt, either Re or W are added to TaMoCrTiAl and their effect on oxidation performance tested at 1000°C in air. To avoid significant changes of the alloy microstructure compared to the reference alloy, in particular the formation of new phases, the amount of the additional element is limited to 3 at.%. The post-test examination and analysis focus on phenomena such as mass gain after given time, thickness and growth of layers in the oxide scale, scale structure and other that are accessible by instruments and methods typically applied to samples after oxidation testing. The priority is to demonstrate the potential of Re or W addition for improving the oxidation performance of Ta–Mo–Cr–Ti–Al alloys. In the following, the alloys with Re or W addition are referred to as TaMoCrTiAl-3Re and TaMoCrTiAl-3W, respectively.

2 | Experimental Procedures

The alloys investigated are produced from the pure metals in the form of granules (Ta, 99.9 wt.%; Ti, 99.7 wt.%; Mo, 99.97 wt.%; Cr, 99.94 wt.%; Al, 99.9 wt.%) or powder (Re, 99.99 wt.%; W, 99.9 wt.%) in an arc melter (model AM/0.5 Arc melting furnace by Edmund Bühler GmbH). The elements are provided in a mass ratio that corresponds to the intended composition, each 20 at.% for the reference alloy TaMoCrTiAl, each 19.4 at.% of the principal elements and 3 at.% Re or W in the case of the modified alloys, at an overall mass between 60 and 100 g. Arc melting is performed under Ar cover gas (around 0.6 atm) in a water-cooled copper mould. The produced alloy buttons are flipped and remelted five times at least, so as to ensure a homogeneous composition of the button. The dendritic microstructure formed during solidification is destroyed by homogenisation for 20 h at 1500°C in a tube furnace (RHTC, Nabertherm GmbH) under flowing Ar. The applied heating and cooling rates are 100 K/h. Spongy titanium is used as a getter to reduce oxygen and nitrogen partial pressure during the heat treatment.

The chemical composition of the alloys is checked after the heat treatment by inductively coupled plasma optical emission spectroscopy (ICP-OES) and energy dispersive X-ray spectroscopy (EDX) in a Zeiss MERLIN scanning electron microscope (SEM). The SEM is operated with an acceleration voltage of 10 keV and beam current between 1 and 5 nA. The phase constitution is analysed by X-ray diffraction (XRD) using Cu $K_{\alpha 1}$ radiation ($\lambda = 0.154$ nm, 40 kV, 30 mA) in a Seifert PAD II diffractometer with Bragg-Brentano geometry (θ–2θ) on samples of approximate dimension $5 \times 5 \times 2$ mm, with surface ground to #1200 and cleaned with ethanol in an ultrasonic bath. The diffraction angles are scanned with a step size of 0.01°, at a speed of 1°/min. For the microscopic analysis of cross-sections, samples are embedded in conductive resin and prepared for investigation in the SEM (grinding to #4000 followed by 1 μm polish). The volume fraction of the phases present and grain size are evaluated in back-scatter electron (BSE) images using the software ImageJ. The former is identified with the percentage of area occupied by the phase in question in the planar image, whereas grain size is determined by the intersection method.

To determine the oxidation kinetics in air at 1000°C, the four alloys are exposed to flowing synthetic air (20.5 vol.% O_2 + 79.5 vol.% N_2, 100 mL/min) in a thermogravimetric system (STA 449 F3 Jupiter, Netzsch-Gerätebau GmbH). Mass change as a function of time is recorded for 72 h. To track the evolution of the structure of the formed oxide scales, further exposures at 1000°C are performed for 48 and 100 h in static laboratory air in a muffle furnace (LT 9/14, Nabertherm GmbH). For each combination of alloy, temperature and time, one sample is tested. For cross-section analysis, oxidised samples are wrapped in Ag and Al foil before embedding and preparation for investigation in the SEM as above. The cross-sections of the oxide scales are analysed in BSE images, supplemented by EDX element mapping and point measurements. The thickness of distinguishable layers in these scales is assessed using ImageJ, by at least 30 measurements in BSE images taken from different locations on the sample. The surface of oxide scales is investigated in secondary electron (SE) mode of the SEM. The analysis of scale cross sections mainly considers the interior of the relatively large alloy grains (> 100 μm), clearly away from the grain boundaries.

For the oxide scales formed during 72 h on TaMoCrTiAl with Re or W addition, a lamella for investigation in the transmission electron microscope (TEM) is prepared by milling with Ga^+ ions in a dual-beam focused ion beam-scanning electron microscope (FiB-SEM, Zeiss Auriga). The TEM and scanning TEM (STEM) investigations are conducted in a FEI Talos F200X operated with 200 kV acceleration voltage. The instrument is equipped with an X-FEG high-brightness electron gun as well as several detectors for STEM imaging: a Thermofisher Ceta 16M CCD camera, a Super-X EDX detector, and a Gatan Enfinium SE spectrometer. Conventional TEM images and diffraction patterns are acquired using the Ceta camera. The orientation of the diffraction pattern is determined using the software SingleCrystal. Electron energy loss spectroscopy (EELS) is employed to track the oxidation states of the cations in the oxides. The Ti-$L_{2,3}$, O-K and Cr-$L_{2,3}$ ionisation edges are captured in a single spectrum with the core-loss region set between 400 and 600 eV at 0.1 eV/channel. For the Ta-$M_{4,5}$ edge, the energy-loss range is set between 1650 and 2100 eV, with a dispersion of 0.25 eV/channel. Low-loss EELS spectra, recorded simultaneously with core-loss data in DualEELS mode, are used for energy-loss calibration and to determine the relative sample thickness t/λ, ensuring that $t/\lambda < 1$ for all analysed spectra. Quantification of the EELS spectra is performed using the built-in cross sections provided by the software Digital Micrograph.

3 | Results

3.1 | Alloy Composition and Microstructure

The chemical compositions of the produced alloys are listed in Table 1. ICP-OES results are in good agreement with the planned compositions. Observed deviations are around 1 at.% or less. EDX with standard-less quantification, the generally less accurate method in contrast to ICP-OES, seems to underestimate especially Mo and correspondingly overestimate others. For the principal elements, EDX differs from ICP-OES results by up to 3 at.%, whereas concentrations indicated for the minor addition correspond to each other within about 1 at.%.

According to the BSE images of cross-sections presented in Figure 1 as well as the XRD patterns in Figure 2, the homogenised alloys are two-phase with the secondary phase C14-type Laves phase (Cr_2Ta), primarily decorating the grain boundaries of the matrix (Figure 1). The latter is body-centred cubic (BCC), ordered B2, though XRD cannot exclude a share of disordered A2 phase as all peaks characteristic for A2 find their counterpart in the B2 pattern (Figure 2). Previous works on TaMoCrTiAl assume B2 [3, 4]. The volume fraction of the Laves phase listed in Table 2 is highest for TaMoCrTiAl (1.5 vol.%), decreases only slightly with the addition of Re and more pronouncedly for W addition (to 0.7 vol.%). All alloys show inter- and intragranular pores (Figure 1). The BCC grain size after homogenisation is significantly smaller in the alloys with Re or W addition, about 1/3 and 1/6, respectively, in comparison to the reference alloy (Table 2). The reduced BCC grain size in the alloys with W or Re addition possibly results from an increase in the number of nuclei forming during the rapid cooling after the arc melting process, which the high melting point of Re and W may suggest. Another possible reason is reduced grain growth during the subsequent homogenisation heat treatment, induced by the presence of the relatively big W or Re atoms in the matrix lattice, in analogy to the interpretation of observations for Co–Cr–Ni medium entropy alloys without and with W addition [12]. In order to reduce

TABLE 1 | Chemical composition in at.% of the alloys investigated: results from ICP-OES and, in brackets, standard-less EDX analysis.

Alloy	Method	Ta	Mo	Cr	Ti	Al	Re	W
TaMoCrTiAl	ICP-OES (EDX)	20.3 (17.9)	20.3 (16.6)	19.7 (22.0)	20.4 (21.0)	19.2 (22.6)		
TaMoCrTiAl-3Re	ICP-OES (EDX)	19.7 (20.8)	19.4 (16.2)	19.5 (20.1)	20.1 (20.3)	18.3 (18.9)	2.8 (3.8)	
TaMoCrTiAl-3W	ICP-OES (EDX)	19.5 (20.9)	19.7 (17.0)	19.4 (19.4)	19.4 (20.1)	18.6 (19.1)		3.0 (3.5)

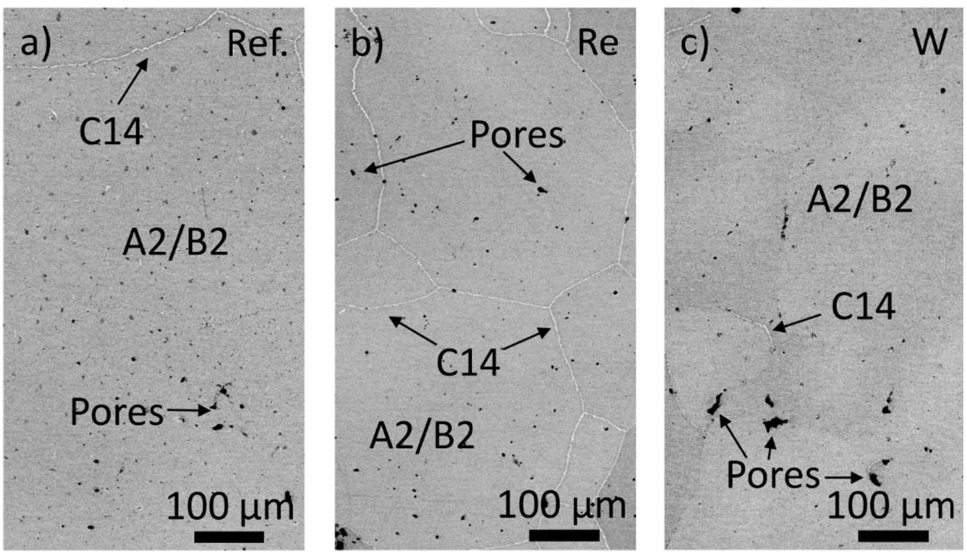

FIGURE 1 | BSE images of the three alloys after heat treatment: (a) TaMoCrTiAl, (b) TaMoCrTiAl-3Re and (c) TaMoCrTiAl-3W.

the influence of these widely varying grain sizes on the quantitative assessment of scale thickness, oxide layer thicknesses are measured in the interior of the BCC matrix grains. This ensures that the observed thicknesses are not influenced by possibly increased diffusion along the matrix-grain boundaries. For the thermogravimetric mass change, which is measured across the entire sample surface, the difference in grain size must indeed be taken into account.

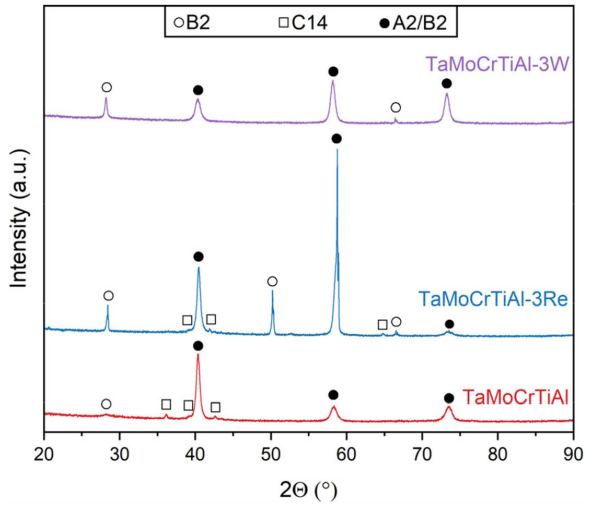

FIGURE 2 | XRD spectra obtained for the three alloys after heat treatment. Peaks specific to the ordered BCC phase B2 are marked by open circles, whereas the closed circles identify peaks common to both B2 and the disordered BCC phase A2. Open squares mark the C14 Laves phase peaks. [Color figure can be viewed at wileyonlinelibrary.com]

TABLE 2 | Volume fraction of C14 Laves phase and average grain size of the BCC matrix as obtained by evaluation of BSE images of the alloys after heat treatment.

Alloy	C14 (vol.%)	BCC grain size (μm)
TaMoCrTiAl	1.5	1178
TaMoCrTiAl-3Re	1.3	367
TaMoCrTiAl-3W	0.7	210

During exposure at 1000°C, the alloys form additional C14 Laves phase, especially inside the matrix grains (Figure 3). Though the method of quantifying the C14 volume fraction relying on the contrast in BSE images works imperfectly if this volume fraction is high and the latter may change from grain to grain, 40–60 vol.% may serve as an indicative number for the reference alloy TaMoCrTiAl after exposure for 48 h (Figure 3a). The corresponding precipitates, in general, have acicular shape (Figure 3a). In the case of TaMoCrTiAl-3Re, new C14 is significantly reduced in some grains (Figure 3b), whereas others show precipitation similar to TaMoCrTiAl. W addition roughly maintains the amount of newly formed Laves phase but alters particle size and shape: On the one hand, the precipitates are more pronouncedly acicular, whereas exceptionally fine and filiform C14 is observed between the relatively long needles (Figure 3c and corresponding inset).

3.2 | Oxide Scale Structure

For analysing the structure and phases present in the oxide scale, samples are available from isothermal exposure for 48 and 100 h in a laboratory furnace as well as for 72 h in the thermogravimetric experiments. This section concentrates on the oxide scales observed on the interior of the BCC matrix grains, whereas scales above the matrix grain boundaries area briefly introduced in the next section.

The general structure of the scales largely complies with earlier reports on the oxidation of Ta–Mo–Cr–Ti–Al alloys [1–4]. The oxides that grow outward in the transient stage of oxidation are TiO_2, Al- and Cr-oxides (Figure 4). Rather than Al_2O_3 and Cr_2O_3 as previously assumed, the element distribution revealed by EDX elemental mapping in the TEM (on TaMoCrTiAl-3W and TaMoCrTiAl-3Re after exposure for 72 h) suggests

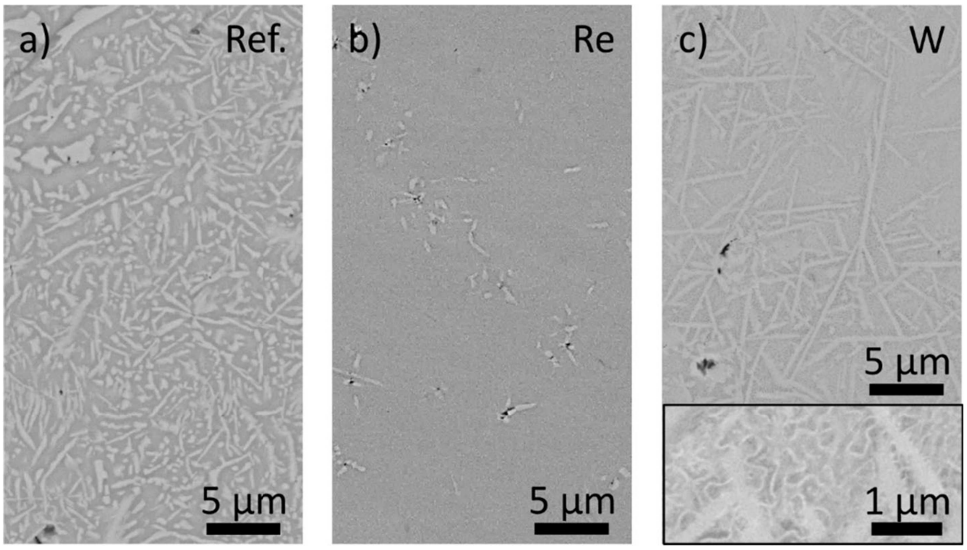

FIGURE 3 | BSE images of the intragranular microstructure after 48 h at 1000°C of alloys (a) TaMoCrTiAl, (b) TaMoCrTiAl-3Re, grain exhibiting reduced C14 precipitation and (c) TaMoCrTiAl-3W.

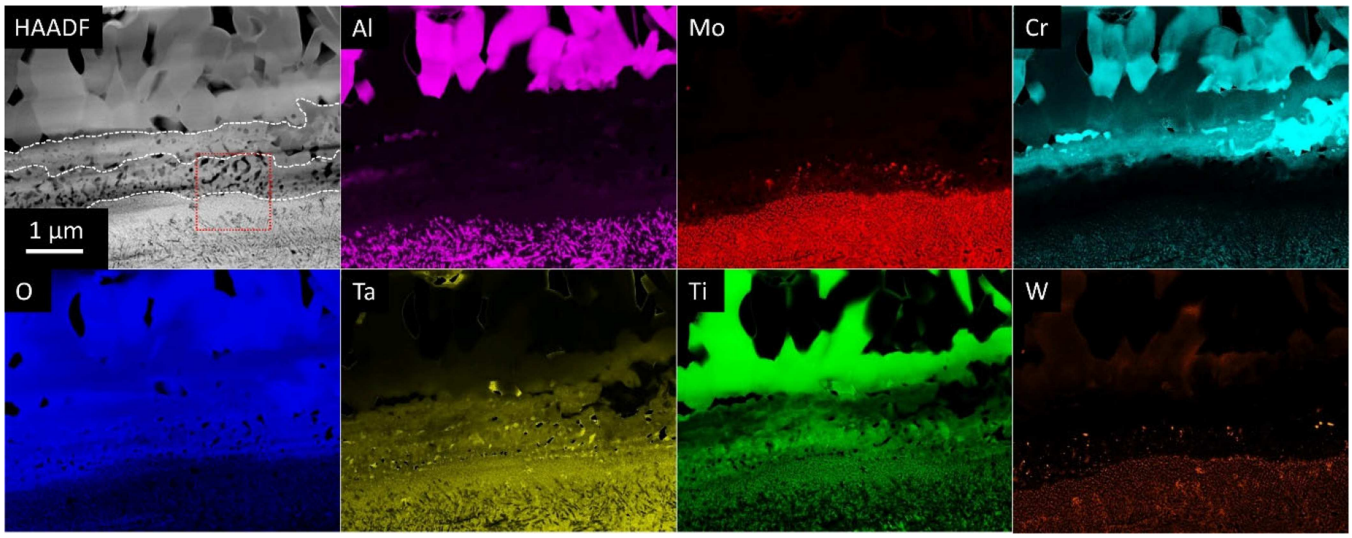

FIGURE 4 | HAADF-STEM micrograph and corresponding EDX elemental mapping of a lamella extracted from the oxide scale on TaMoCrTiAl-3W after exposure for 72 h to synthetic air at 1000°C. The outer part of the oxide scale consists of TiO_2 and $(Al,Cr)_2O_3$ solid solution, whereas the centre portion (marked by dashed lines) primarily is $(Cr,Ta,Ti)O_2$ and $(Ti,Ta)O_2$, respectively. The alloy underneath these layers especially shows precipitated Al_2O_3. The area marked in red is shown in more detail in Figure 5. [Color figure can be viewed at wileyonlinelibrary.com]

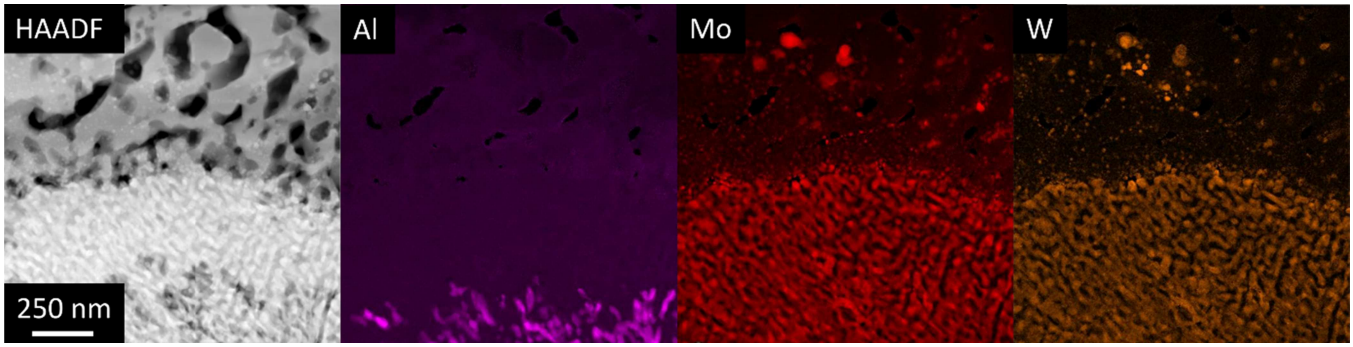

FIGURE 5 | HAADF-STEM micrograph and selected EDX elemental mapping of a section of the lamella analysed in Figure 4 that comprises the $(Ti,Ta)O_2$ layer and transition to internal corrosion. [Color figure can be viewed at wileyonlinelibrary.com]

$(Al,Cr)_2O_3$ solid solutions, with concentration of Al and Cr varying for individual grains. TiO_2 can be found above, but also underneath the $(Al,Cr)_2O_3$ solid solution (Figure 4). The layer adjacent to the outer oxide shows the elements characteristic for $(Cr,Ta,Ti)O_2$, the complex oxide described earlier [1]. It contains Cr_2O_3 inclusions, mainly located close to the interface with the outer oxide layer. Such inclusions grow with increasing exposure time, preferentially laterally at the mentioned interface, forming a discontinuous layer in some spots (Figure 4). The other of the two layers forming the centre part of the scale rather complies with $(Ti,Ta)O_2$, with a few tens of nm sized metallic particles, which are Mo-rich (Figure 4). This layer descends to a zone of internal corrosion with exceptionally fine-grained transition. This transition is depleted in Al as deduced from the Al map presented in Figure 5, for example, in comparison to the Mo map. Other constituent elements of the alloys do not show comparable depletion. The examination of all samples in the SEM corroborates the general structure of the oxide scale and phases present above the zone of internal oxidation. A roughly noticeable difference for TaMoCrTiAl-3Re or TaMoCrTiAl-3W in comparison to the alloy without addition is a somewhat thicker fine-grained transition from dominant $(Ti,Ta)O_2$ to internal corrosion (~500 nm in Figure 5). A clearer manifestation of the small addition to TaMoCrTiAl, notably of W, is the enrichment of W in the Mo-base particles included in $(Ti,Ta)O_2$, as apparent from the STEM/EDX results in Figure 4, and especially from Figure 5. Such correspondence in the distributions of W and Mo is also observed for Re and Mo, as revealed by TEM-EDX elemental mapping of the scale formed on TaMoCrTiAl-3Re (Figure 6). Corresponding bright spots in the Mo and Re map clearly signify Mo–Re particles in $(Ti,Ta)O_2$.

The two distinguished layers of rutile-base oxide may also be deduced from TEM on TaMoCrTiAl after oxidation at 1200°C, though not particularly addressed in the respective study [1]. Not clearly separable in SEM images, both layers are collectively referred to as complex oxides when, in the following, observations in SEM images are introduced.

The oxide scales in their entirety reflect the dominance in terms of corrosion depth of internal corrosion over the formation of external oxide layers (Figure 7). The precipitates are predominantly Al_2O_3 as qualitatively identified by EDX. The inset also shows the Laves phase that forms during the exposure at 1000°C, which appears bright in the BSE micrograph, and

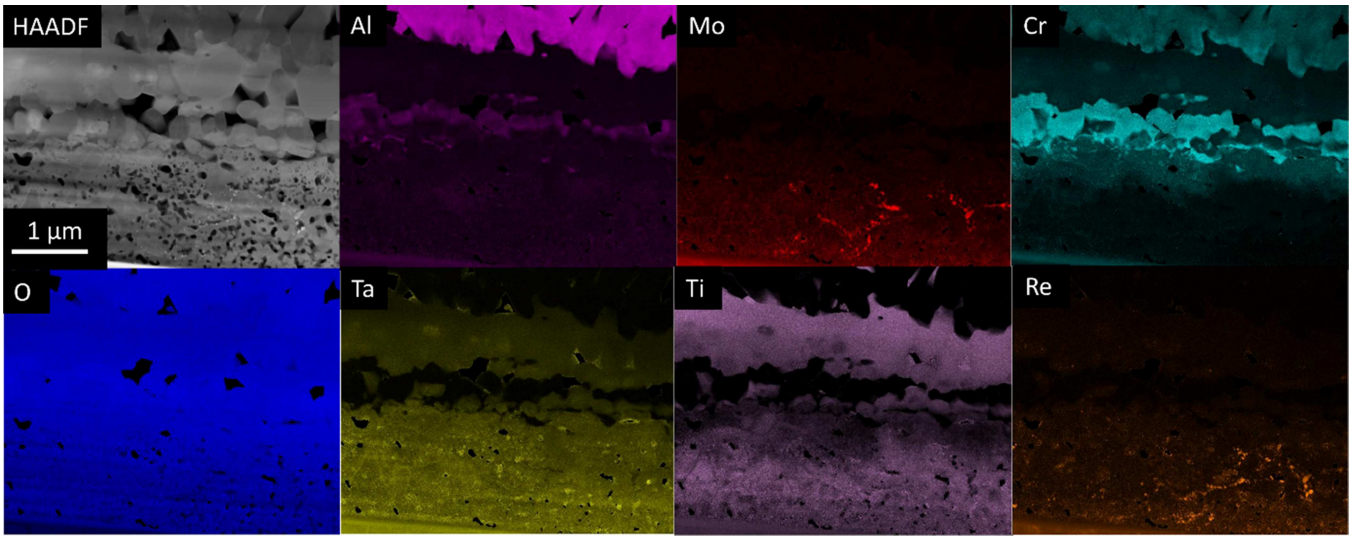

FIGURE 6 | HAADF-STEM micrograph and corresponding EDX elemental mapping of a lamella extracted from the oxide scale on TaMoCrTiAl-3Re after exposure for 72 h to synthetic air at 1000°C. The upper part of the frame shows the $(Al,Cr)_2O_3$ solid solution, in the centre primarily $(Cr,Ta,Ti)O_2$ with some embedded Cr_2O_3 grains and at the bottom $(Ti,Ta)O_2$ with small Mo and Re inclusions. [Color figure can be viewed at wileyonlinelibrary.com]

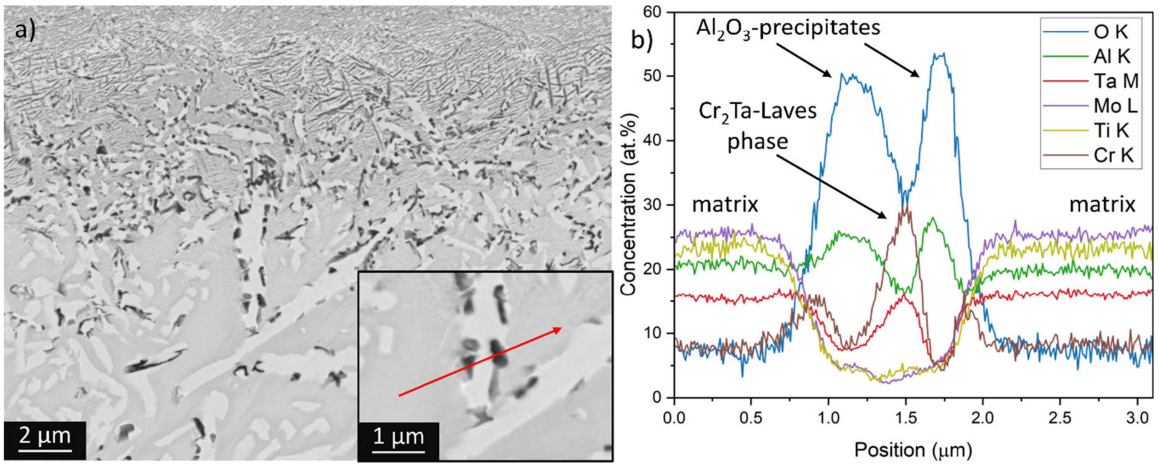

FIGURE 7 | Internal oxidation formed on TaMoCrTiAl after exposure for 48 h to laboratory air at 1000°C. (a) BSE micrograph. (b) EDX-line scan at position indicated by red line in the inset in (a). [Color figure can be viewed at wileyonlinelibrary.com]

precipitates (dark) preferentially nucleating on the Laves phase particles. In addition to Al_2O_3, SEM-EDX elemental mappings suggest the presence of TiN precipitates for all samples, which would be in line with previous findings [2–4]. In detail, the observed internal corrosion zones have, more or less pronouncedly, different appearance. Taking the respective zone formed during 100 h in TaMoCrTiAl (Figure 8a) as the benchmark, the local number density or volume fraction of precipitates may be somewhat lower (Figure 8b) or, as exemplified with TaMoCrTiAl-3W after the same exposure time, seems significantly higher (Figure 8c). In the latter case, the best part of the internal corrosion zone holds exceptionally small precipitates, which are Al-rich. At the transition to the alloy, TiN formation is dominant in all cases, progressing into the alloy along the acicular Laves phase (Figure 8). The evaluation of various internal corrosion zones corroborates that if the part characterised by fine precipitates with high number density is relatively pronounced, comparable to Figure 8c, the internal corrosion zone overall is comparatively thin. Laves phase, if present in this portion of the internal corrosion zone, is observed in the form of small, scattered particles rather than in the typical acicular habitus. Internal corrosion with pronounced contribution from the fine precipitates is characteristic for TaMoCrTiAl-3W, whereas for the reference alloy, their domain in the internal corrosion zones mostly is relatively small. In the case of TaMoCrTiAl-3Re, both grains with minor C14 Laves phase formation during the exposure (cf. Figure 3b) and the others may show a prominent share of the fine precipitates in the internal corrosion zone.

The top view of the oxide scales (Figure 9) shows the largely equiaxed oxide grains seen in the sample cross sections as protruding from the surface. For the reference TaMoCrTiAl, single crystallites are still distinguishable after 72 h (Figure 9a), whereas the topography observed on TaMoCrTiAl-3Re after the same time rather suggests that gaps between crystallites already closed, smoothening the surface (Figure 9b). TaMoCrTiAl-3W

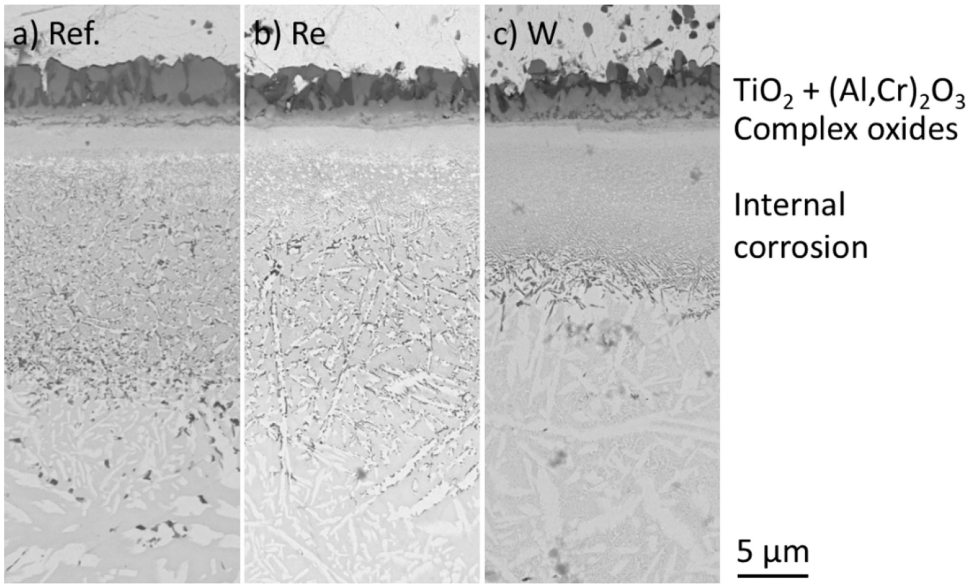

FIGURE 8 | Cross-section of oxide scales formed on (a) TaMoCrTiAl, (b) TaMoCrTiAl-3Re and (c) TaMoCrTiAl-3W during isothermal exposure for 100 h to laboratory air at 1000°C.

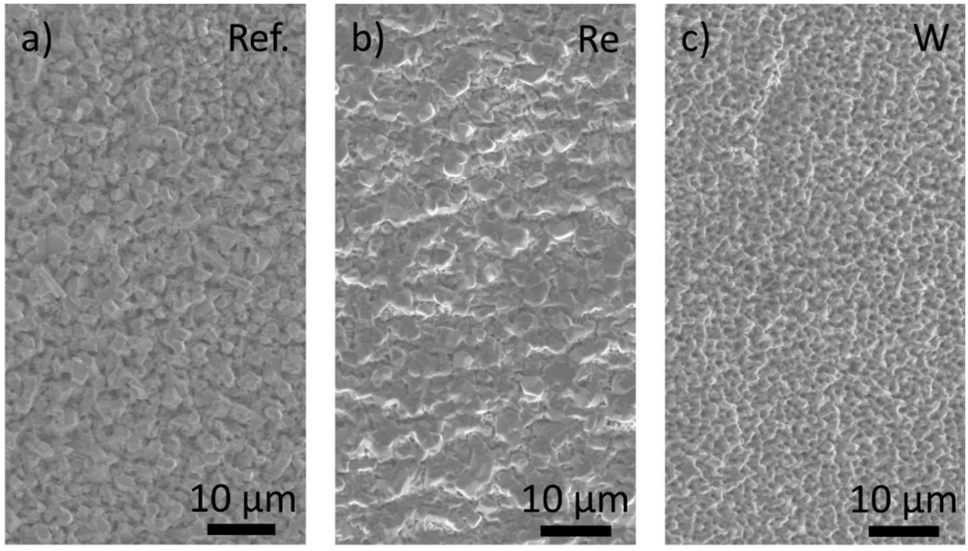

FIGURE 9 | Surface of oxide scales formed during isothermal exposure for 72 h to synthetic air at 1000°C on (a) the reference TaMoCrTiAl alloy as well as on modified alloys (b) TaMoCrTiAl-3Re and (c) TaMoCrTiAl-3W.

also still shows the habitus of crystals that in contrast to TaMoCrTiAl, have clearly reduced size (Figure 9c).

3.3 | Scales Above the Matrix Grain Boundaries

The grain boundaries of the BCC matrix of the alloys typically are decorated with C14 Laves phase already in the state before exposure to air at 1000°C. In general, an oxidation performance different from the interior of BCC grains can be expected. As exemplified with Figure 10a, such difference is of quantitative rather than qualitative nature. The external oxides tend to be somewhat thicker, whereas internal corrosion proceeds deeper into the alloy along the relatively coarse Laves particles. Inward growth anticipated for the complex oxides consumes the Laves phase. Figure 10b indicates that mild spalling and buckling are possible above the BCC matrix grain boundaries.

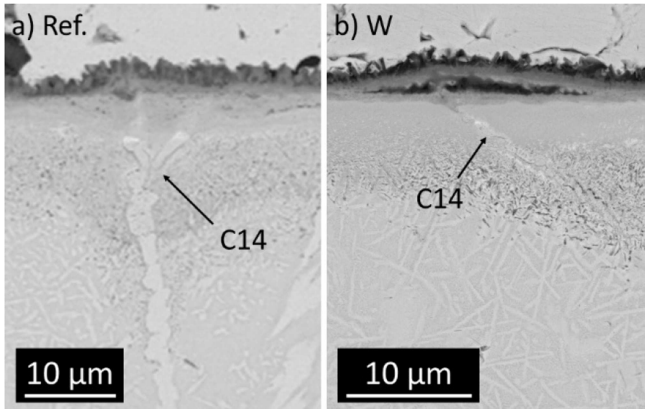

FIGURE 10 | Scales after exposure for 48 h at 1000°C above matrix grain boundaries in (a) TaMoCrTiAl and (b) TaMoCrTiAl-3W.

3.4 | Mass Change and Scale Thickness

Figure 11 presents the area-specific mass change observed in the thermogravimetric experiments for 72 h. The linear regression in a double-logarithmic plot of recorded mass change over time yields exponents n in a general potential law that range from 1.83 (TaMoCrTiAl) to 1.99 (TaMoCrTiAl-3Re), close enough to assume parabolic mass gain in the early period of oxidation at 1000°C. Parabolic rate constants k_p resulting from fitting parabolic rate laws to the calculated area-specific change as a function of time are between 1.9×10^{-2} (TaMoCrTiAl-3Re) and 2.7×10^{-2} mg^2/cm^4 h (TaMoCrTiAl). The mass gain after 72 h obtained for the reference alloy TaMoCrTiAl is about 20% higher than observed for the modified alloys, about 10% higher for TaMoCrTiAl-3W in comparison to TaMoCrTiAl-3Re. The data characterising the alloys in terms of mass change during oxidation at 1000°C in air are summarised in Table 3. The observations for the alloy without addition comply fairly well with a previous study [4].

Corresponding scale thickness as measured in BSE micrographs is compiled in the right part of Figure 12 (Thermobalance, 72 h). Overall thickness including internal corrosion qualitatively reflects higher mass gain of TaMoCrTiAl in comparison to the modified alloys. The notion of less oxidation in TaMoCrTiAl-3Re than in the W-containing variant is, however, not confirmed. This leads to the impression that at least in the case of the type of alloys investigated, a difference of 10% observed in mass gain is not yet significant enough for a qualitative ranking in terms of degradation. Estimating from the inward growing complex oxides and internal corrosion an average (intragranular) corrosion depth suggests 17 and 14 μm after 72 h for TaMoCrTiAl-3Re and TaMoCrTiAl-3W, respectively. Considering the spread in singular measurements as indicated by the error bars in Figure 12, approximately same or even slightly smaller corrosion depth in TaMoCrTiAl-3Re may be found if the two alloys are locally compared. Moreover, this applies only if the behaviour at grain boundaries is taken into account (cf. Section 3.3). Somewhat thicker oxide and deeper internal corrosion at the grain boundaries should have greater effect on the mass gain of TaMoCrTiAl-3W, which has the smaller BCC matrix grains (Table 2) and, therefore, more grain boundaries per unit of surface area. Another potential reason for higher mass gain though a thinner scale thickness, especially the internal corrosion zone, is a higher volume fraction of precipitates forming in the course of internal oxidation.

Figure 12 also shows the thickness of the layers in the oxide scale found after exposure in the muffle furnace. After 48 h, the general trends in terms of average overall thickness and corrosion depth, respectively, qualitatively correspond to the thermogravimetric experiments. Taking into account that the latter ran 72 h, the complex oxide layer is generally thicker in the furnace test and especially the local variation in the thickness of the internal corrosion scale is smaller. Mainly due to a

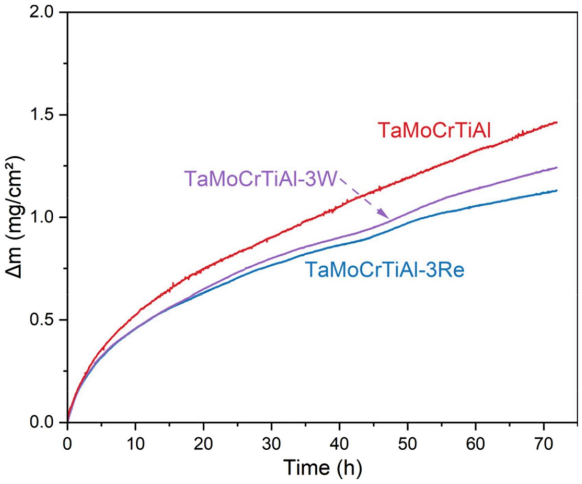

FIGURE 11 | Area specific mass change as a function of time during isothermal exposure of the investigated alloys to synthetic air at 1000°C. [Color figure can be viewed at wileyonlinelibrary.com]

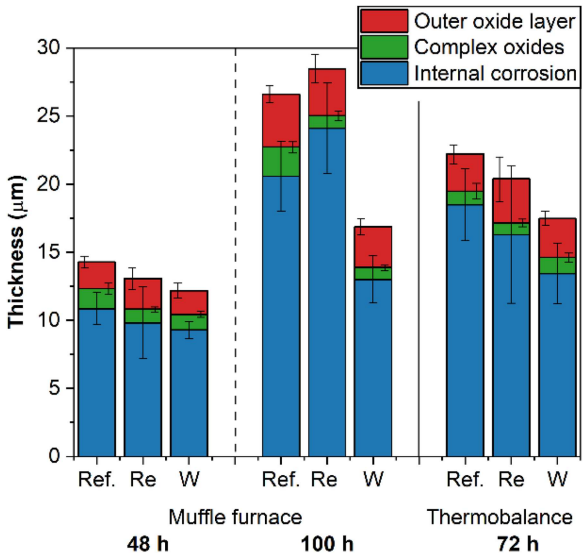

FIGURE 12 | Thickness of distinguishable layers in the oxide scale observed on TaMoCrTiAl (ref.) and the alloys with addition of 3 at.% Re and W, respectively, after exposure at 1000°C in air, in the muffle furnace and thermobalance, respectively. For the interior of BCC matrix grains and measured in BSE micrographs. [Color figure can be viewed at wileyonlinelibrary.com]

TABLE 3 | Rate-law exponent n, parabolic rate constant k_p and mass gain after 72 h observed for oxidation of TaMoCrTiAl, TaMoCrTiAl-3Re and TaMoCrTiAl-3W at 1000°C in synthetic air. Furthermore, the average intragranular corrosion depth deduced from BSE micrographs is listed.

Alloy	n (−)	k_p (10^{-2} mg^2/cm^4 h)	Mass gain, 72 h (mg/cm^2)	Depth, 72 h (μm)	Reference
TaMoCrTiAl	1.83	2.7	1.46	20	This study
TaMoCrTiAl	1.82	3.3			[4]
TaMoCrTiAl-3Re	1.99	1.9	1.13	17	This study
TaMoCrTiAl-3W	1.89	2.1	1.24	14	This study

disproportionate increase in internal corrosion, the furnace test for 100 h reveals an overall thicker scale for TaMoCrTiAl-3Re in comparison to the alloy without addition. The indicated scale growth for TaMoCrTiAl-3W is comparatively moderate, and affects the outer oxide layer and internal oxidation zone roughly in proportion to their thickness after 48 h. Intragranular scale growth as observed in the furnace test for 48 and 100 h also contradicts the impression of relative oxidation performance of the alloys gained from the thermogravimetric curves recorded for 72 h.

3.5 | In-Depth Analysis of $(Ti,Ta)O_2$ and $(Cr,Ta,Ti)O_2$ Layers

An in-depth analysis of oxide layers is performed on TaMoCrTiAl-3W after oxidation for 72 h. For the Ti- and Ta-rich portion of the scale, selected area diffraction (SAED) reveals rutile-type $(Ti,Ta)O_2$ (Figure 13). The rutile structure is also confirmed for the $(Cr,Ta,Ti)O_2$ layer (not shown here, as already reported earlier [1, 4]).

STEM-EDX identifies the elements dominating these layers (Figure 14). Mo and W in the $(Ti,Ta)O_2$ layer, order of 5 at.% overall (Table 4), is likely to correspond to the metallic particles mentioned earlier in the text. The EDX spectra in Figure 14b and results of quantification in Table 4 especially point to the prominent difference in Cr content between the two oxides in the inner layers of the scale. Assuming some credibility of the quantification as to the atom ratio of metal cations in the oxides, the indicative numbers following are about 1:1.1:1.5 and 1:1.3 for Ta:Cr:Ti in $(Cr,Ta,Ti)O_2$ and Ta:Ti in $(Ti,Ta)O_2$, respectively.

STEM-EELS spectra acquired from the TaMoCrTiAl-3W lamella in two ranges of energy-loss are presented as Figure 14c,d. Figure 14c shows the energy-loss range from 450 to 600 eV where the Ti-$L_{2,3}$, O-K and Cr-$L_{2,3}$ edges are located. Besides the presence/absence of Cr-related features, the energy loss near-edge structure (ELNES) of the Ti-$L_{2,3}$ and O-K edge differs for $(Cr,Ta,Ti)O_2$ and $(Ti,Ta)O_2$, most notably for the Ti-$L_{2,3}$ edge. For $(Ti,Ta)O_2$, the peak shape in the Ti position corresponds to a formal valence of +3, whereas +4 is indicated for $(Cr,Ta,Ti)O_2$ [13, 14]. Adopting the method of Zanetta et al. [15], the Ti^{4+} atom fraction with reference to the sum over all Ti^{x+} is 0.0 and 0.86 for $(Ti,Ta)O_2$ and $(Cr,Ta,Ti)O_2$, respectively. Figure 15 shows EELS measurements for the complex oxides formed on TaMoCrTiAl-3Re, which confirm this variability in the valence of Ti. The positions of the O-K edge peaks are nearly the same for both oxides (Figure 14c), and observed differences are largely confined to the second peak but appear too subtle to interpret at this stage. For Cr in $(Cr,Ta,Ti)O_2$, the corresponding EELS spectrum clearly suggests a valence of +3 [16]. Energy loss in the range from 1650 to 2100 eV, which includes the Ta-$M_{4,5}$ edge, appears similar for both oxides (Figure 14d) and implies a valence of +5 for Ta in both oxides [1]. The Re-M and W-M edges overlap with the Ta-M edge so that the determination of the valence of Re and W in the $(Ti,Ta)O_2$ layer is not possible with EELS, given the small concentration of these elements in this layer.

4 | Discussion

The results from thermogravimetry show that for 72 h at 1000°C in air, adding 3 at.% of Re or W to TaMoCrTiAl, qualitatively has the positive effect on oxidation performance, for example, reduced mass gain, that could be expected if these elements are incorporated into the protective $(Cr,Ta,Ti)O_2$ as cations of valence > +4. This the more so applies if the significantly smaller grain size of the alloys with minor additions is taken into account. The notion that Re addition seems to be slightly more beneficial to the oxidation performance than W reverses if scales on and corresponding corrosion depth in the interior of matrix grains are considered. More important than potential reasons for this (cf. Section 3.4) is the observation that in the furnace test for 100 h any beneficial effect of Re addition on the overall oxidation performance has vanished, but still persists in the case of W. The driver of alloy degradation certainly is internal corrosion, as also found in earlier oxidation tests on TaMoCrTiAl [4]. The increase of internal corrosion between 48 and 100 h of oxidation time is especially pronounced in TaMoCrTiAl-3Re.

One of the implications of this work as to how Re or W act on the oxidation mechanism of TaMoCrTiAl is their enrichment in Mo-base metallic particles in the complex oxides, notably in the

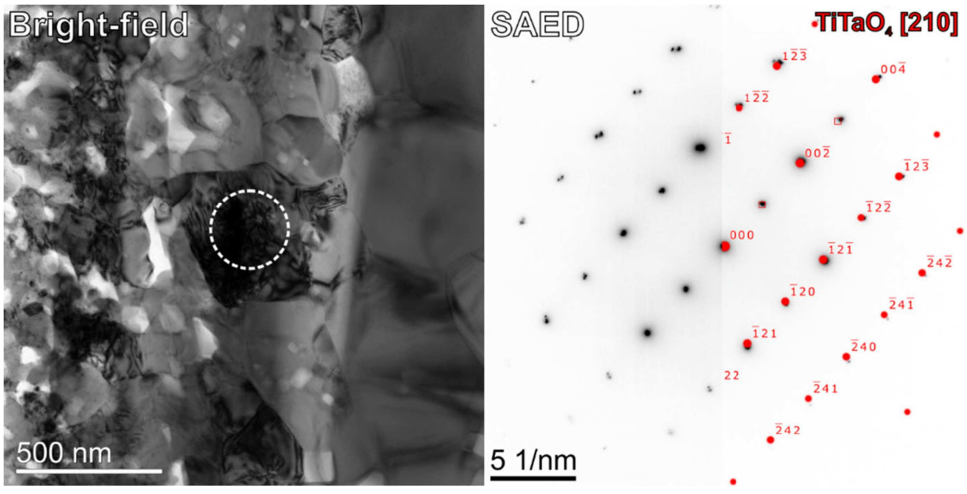

FIGURE 13 | Bright-field TEM image with corresponding selected area diffraction pattern (SAED) of a grain in the intermediate Ta- and Ti-rich oxide layer. The grain has been identified as $TiTaO_4$ (or $(Ti,Ta)O_2$) phase of rutile structure as is seen by superimposition of the simulated $TiTaO_4$ pattern. [Color figure can be viewed at wileyonlinelibrary.com]

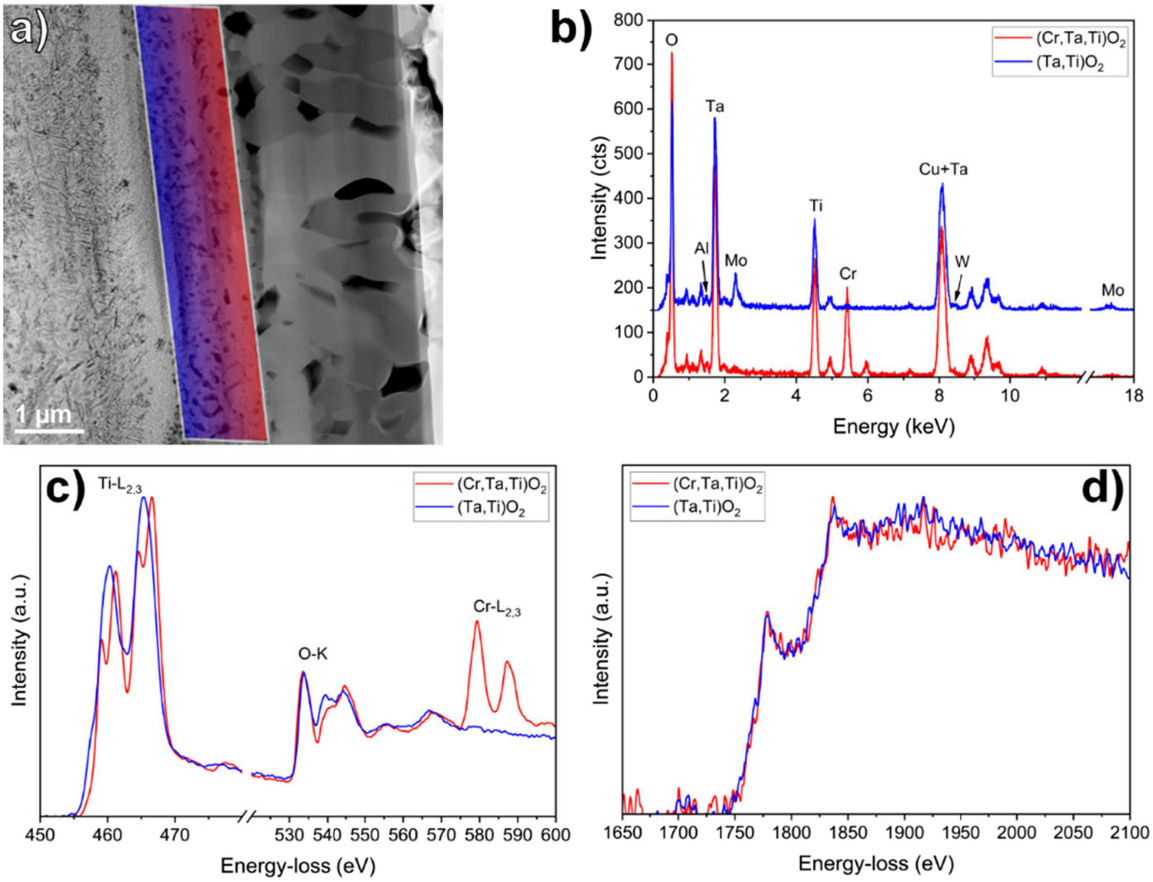

FIGURE 14 | Results from TEM investigation of complex oxide layers on TaMoCrTiAl-3W: (a) STEM-HAADF image with regions of interest highlighted in blue and red, marking low and high Ti^{4+} content, respectively; (b) STEM-EDX spectra; (c) EELS spectra including Ti-L, O-K and Cr-L edges; and (d) EELS spectra showing the Ta-M edges. STEM-EDX and EELS spectra were acquired from the same spots in the blue and red regions, respectively. [Color figure can be viewed at wileyonlinelibrary.com]

TABLE 4 | Results from quantitative STEM-EDX (in at.%) performed on the $(Cr,Ta,Ti)O_2$ and $(Ti,Ta)O_2$ layers, as following from the spectra in Figure 14b.

Layer	Ta	Mo	Cr	Ti	Al	W	O
$(Cr,Ta,Ti)O_2$	7.5	0.9	8.3	11.1	0.5	0.3	71.4
$(Ti,Ta)O_2 + (Mo,W)$	9.5	4.0	0.5	12.5	0.7	0.6	72.3

newly uncovered $(Ti,Ta)O_2$ portion. Though not yet considered being first retained in the complex oxides, Mo volatilisation in the form of oxide [1, 4] is still likely to play a role in the process of oxidation, with which the additions to the alloy may interfere. The TEM work proves such local enrichment in the complex oxides for both alloys with W or Re addition. Further TEM work is required for deciding on the significance of the noticed influence of Re and W on the thickness of the thin transition zone between the complex oxide and internal oxidation. Another possible way the additions to TaMoCrTiAl, especially W, may have influenced the overall oxidation performance is seen in the establishment of the near-surface portion of the internal oxidation zone that is comparatively densely populated by precipitates, oxides and/or nitrides (Figure 8c). The role of W in this could be the promotion of precipitate growth and especially nucleation through lowering the solubility product of the precipitating phase (higher degree of supersaturation for the same concentrations in the alloy). W addition reducing the solubility of oxygen or nitrogen in the alloy is the necessary prerequisite, which may be deduced from the comparatively low solubility of the non-metals in pure W [17, 18]. The high number density and volume fraction of precipitates then resulting is an obstacle for diffusion of oxygen and nitrogen into the alloy, as frequently discussed in connection with TiN [19–22]. Similarly, the relatively fine-grained Laves phase that tends to precipitate in TaMoCrTiAl-3W grains simultaneously with internal corrosion may work towards reduced depth of internal corrosion. Certainly, needing more experimental evidence, the impediment to progress of internal corrosion seems a more persistent influence on overall performance in contact with air at high temperature than an effect via the volatilisation of the Mo particles, which could be a decisive difference between Re and W addition, rendering the beneficial effect of the former less durable.

As for the anticipated doping of the complex oxides, $(Cr,Ta,Ti)O_2$ as well as $(Ti,Ta)O_2$ with Re^{7+} or W^{6+} cations, it could be argued that if a significant part of 3 at.% of the corresponding elements in the alloy accumulates in metallic inclusions, the percentage actually ending up in the complex oxides may be rather small, but not necessarily too small to noticeably influence the oxygen vacancy concentration. Furthermore, a fraction of the already reduced amount incorporated into the oxide may possibly have +4 valence, corresponding to oxides ReO_2 and WO_2, without effect on the defect concentration in the anion sublattice. Nevertheless,

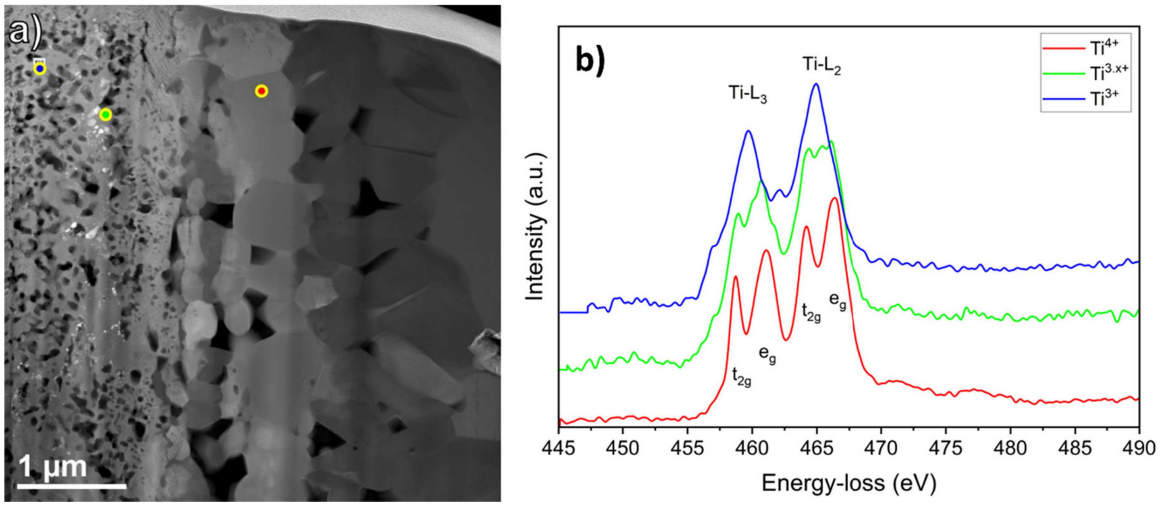

FIGURE 15 | Results from TEM investigation of complex oxide layers formed on TaMoCrTiAl-3Re. (a) STEM-HAADF image with spots of EELS measurements on $(Cr,Ta,Ti)O_2$ (red), $(Ti,Ta)O_2$ (blue) and an intermediate position (green). (b) EELS spectra of Ti-L peaks. [Color figure can be viewed at wileyonlinelibrary.com]

at least in the furnace tests, less growth of the complex oxides in contrast to the alloy without addition is observed (Figure 12), despite the grain boundaries, inclusions and pores (Figures 4, 5, 13 and 14) that offer diffusion paths alternative to the interior of oxide grains, which should be primarily affected by doping. Hence, oxidation of the investigated alloys is highly complex and clear conclusions on the significance of the anticipated doping effect for beneficial performance on the basis of the observations so far available are difficult. It may, however, be concluded that the derived positive effect of W on internal corrosion will benefit from reduced cation transport in the complex oxide, but reduced cation transport in the complex oxide is probably not a necessary prerequisite for a positive effect of W addition on the internal corrosion. Considering the performance of TaMoCrTiAl-3Re, a beneficial effect of oxide doping on overall oxidation performance, if initially significant, may finally be only of short duration.

The identification of $(Ti,Ta)O_2$ interspersed with Mo-rich metallic particles underneath $(Cr,Ta,Ti)O_2$ is considered a valuable by-product of the analytical work on the oxide scales formed on the investigated Ta–Mo–Cr–Ti–Al alloys. Experimental evidence as regards the sequence of formation of these two layers is not yet available, but it could be argued that $(Ti,Ta)O_2$ may generally form underneath an already existing $(Cr,Ta,Ti)O_2$ layer, as the oxygen activity needed for this oxide to establish is lower [22]. Cr consumption through formation of $(Cr,Ta,Ti)O_2$ along with insufficient re-supply from the alloy then triggers the change in oxide composition. However, if Cr is mobile in the $(Ti,Ta)O_2$, this oxide may form first, and Cr accumulates in the long run where the higher oxygen activity prevails, that is, on the side opposite to the alloy. The transition between the two corresponding domains of the oxide scale is gradual (Figure 14a), complying with both potential routes of establishment suggested. For ternary Ta–Cr–Ti alloys, the formation of $(Ti,Ta)O_2$ is assigned the role of suppressing deleterious Ta_2O_5 formation [23, 24].

Evaporation of Mo in the form of MoO_3 [4] becomes more likely the closer to the oxide scale/gas interface it occurs, where open porosity in the scale allows oxygen and gaseous MoO_3 to enter and leave, respectively. In the interior of the scale, notably inside the $(Ti,Ta)O_2$

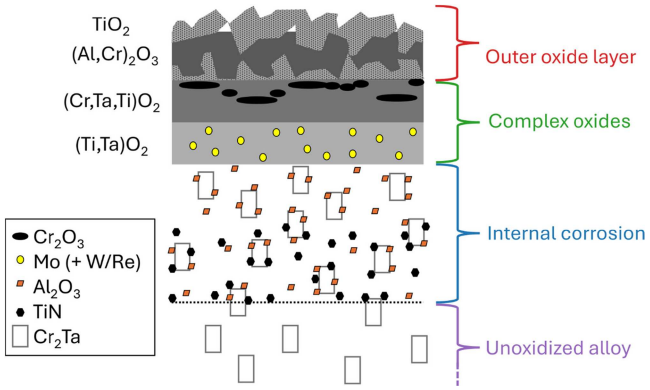

FIGURE 16 | Schematic illustration of the oxide scale formed on TaMoCrTiAl, TaMoCrTiAl-3Re and TaMoCrTiAl-3W during exposure at 1000°C in air. [Color figure can be viewed at wileyonlinelibrary.com]

layer, oxygen activity is not high enough for solid Mo-containing oxide and the MoO_3 partial pressure is significantly reduced, leading to the observed Mo accumulation in the metallic particles. Another detail of potential relevance to a complete mechanistic understanding of oxide scale formation on the complex alloys pertains to TiO_2 in the outer oxide layer. The position in which this oxide is primarily observed varies is the interface with $(Cr,Ta,Ti)O_2$ (Figure 4) or the top of the outer oxide layer (Figure 6). Furthermore, it fills the gaps between the $(Al,Cr)_2O_3$ crystallites. Comparing the thermodynamic stability of Al_2O_3 and TiO_2, the top of the scale is the position that should be favoured by TiO_2. Hence, the Ti maps in Figures 4 and 6 may represent two states of the establishment of TiO_2 in the outer oxides, that is, the formation mostly underneath or between the $(Al,Cr)_2O_3$ crystallites in the transient stage and subsequent accumulation on top of the scale. The top view that corresponds to Figure 6 (Figure 9c) corroborates the notion that crystallites, typically forming in contact with the gas phase, have been overgrown. Though observed clearest for the scale on TaMoCrTiAl-3Re, reordering of TiO_2 in the outer oxide is likely to be a general feature in the oxidation of Ta–Mo–Cr–Ti–Al alloys, because it is driven by thermodynamic forces that are independent of the presence of Re in the alloy.

Figure 16 expands earlier illustrations of the general structure of oxide scales formed on Ta–Mo–Cr–Ti–Al alloys at 1000°C in air [4] by the new findings of this study.

5 | Conclusions

- Addition of 3 at.% of either Re or W to equimolar Ta–Mo–Cr–Ti–Al is beneficial to the oxidation performance at 1000°C in air, at least temporarily. The positive effect is noticeable especially in the reduced thickness of the internal corrosion zone.
- For the Re addition, the beneficial effect is short term, and has vanished after 100 h. It is more persistent in the case of W, attributed to a positive impact on the structure and development of the internal oxidation zone.
- The predictive power of the classic theory of doping protective oxides is limited in the case of the complex alloys. As to the influence of W, doping of rutile-type oxide such as $(Cr,Ta,Ti)O_2$ may contribute to but cannot be clearly confirmed and, if applicable, is unlikely to be the only reason for improved oxidation performance.
- Another constituent part with rutile structure has been identified in the oxide scale on the complex alloys, namely $(Ti,Ta)O_2$, with +3 and +5 valence of the Ti and Ta cations, respectively. Metallic Mo inclusions in this oxide confirm the inward growth of the complex oxides.

Acknowledgments

Funding by the Deutsche Forschungsgemeinschaft (DFG) under grant 467750555 is gratefully acknowledged. The authors would like to thank Dr. T. Bergfeldt for chemical analyses of the investigated materials. Furthermore, the opportunity of using analytical instruments of the Metallic Materials and Thin Film departments of IAM-AWP is gratefully acknowledged. This study was supported by the Deutsche Forschungsgemeinschaft (DFG, German Research Foundation) under grant number 467750555. Open Access funding enabled and organized by Projekt DEAL.

Conflicts of Interest

The authors declare no conflicts of interest.

Data Availability Statement

The data that support the findings of this study are available from the corresponding author upon reasonable request.

References

1. S. Schellert, M. Weber, H. J. Christ, et al., "Formation of Rutile $(Cr,Ta,Ti)O_2$ Oxides During Oxidation of Refractory High Entropy Alloys in Ta-Mo-Cr-Ti-Al System," *Corrosion Science* 211 (2023): 110885.

2. S. Schellert, B. Gorr, S. Laube, A. Kauffmann, M. Heilmaier, and H. J. Christ, "Oxidation Mechanism of Refractory High Entropy Alloys Ta–Mo–Cr–Ti–Al With Varying Ta Content," *Corrosion Science* 192 (2021): 109861.

3. B. Gorr, F. Müller, S. Schellert, et al., "A New Strategy to Intrinsically Protect Refractory Metal Based Alloys at Ultra High Temperatures," *Corrosion Science* 166 (2020): 108475.

4. F. Müller, B. Gorr, H.-J. Christ, et al., "On the Oxidation Mechanism of Refractory High Entropy Alloys," *Corrosion Science* 159 (2019): 108161.

5. C. Tang, B. Schäfer, C. Schroer, and B. Gorr, "Improved Oxidation Behavior of M-20Cr-20Ta (M: Ni, Fe, Co) Ternary Alloys by Formation of Complex Cr–Ta-Based Oxides," *Corrosion Science* 249 (2025): 112847.

6. M. Louis Etienne, G. Stéphane, L. Guillaume, and M. Hideyuki, "Microstructure and Oxidation Behavior of Co-Cr-Ta Ternary Alloys," *Journal of Alloys and Compounds* 936 (2023): 167968.

7. W. Ren, F. Ouyang, B. Ding, et al., "The Influence of CrTaO4 Layer on the Oxidation Behavior of a Directionally Solidified Nickel-Based Superalloy at 850-900°C," *Journal of Alloys and Compounds* 724 (2017): 565–574.

8. K. Khanchych, C. Tang, C. Schroer, et al., "CALPHAD-Guided Prediction and Interpretation of Phase Formation in Ta–Mo–Cr–Ti–Al Refractory High-Entropy Alloys," *Advanced Engineering Materials* 27 (2025): 2500527.

9. N. Birks, G. H. Meier, and F. S. Pettit, *Introduction to the High Temperature Oxidation of Metals* (Cambridge University Press, 2006).

10. P. Kofstad, *High Temperature Corrosion* (Elsevier Applied Science, 1988).

11. K. Hoshino, N. L. Peterson, and C. L. Wiley, "Diffusion and Point Defects in TiO_{2-x}," *Journal of Physics and Chemistry of Solids* 46 (1985): 1397–1411.

12. R. Chang, W. Fang, X. Bai, et al., "Effects of Tungsten Additions on the Microstructure and Mechanical Properties of CoCrNi Medium Entropy Alloys," *Journal of Alloys and Compounds* 790 (2019): 732–743.

13. E. Stoyanov, F. Langenhorst, and G. Steinle-Neumann, "The Effect of Valence State and Site Geometry on Ti $L_{3,2}$ and O K Electron Energy-Loss Spectra of Ti_xO_y Phases," *American Mineralogist* 92 (2007): 577–586.

14. L. F. Kourkoutis, H. L. Xin, T. Higuchi, et al., "Atomic Resolution Spectroscopic Imaging of Oxide Interfaces," *Philosophical Magazine* 90 (2010): 4731–4749.

15. P.-M.- Zanetta, V. R. Manga, Y.-J. Chang, et al., "Atomic-Scale Characterization of the Oxidation State of Ti in Meteoritic Hibonite: Implications for Early Solar System Thermodynamics," *American Mineralogist: Journal of Earth and Planetary Materials* 108 (2023): 881–902.

16. T. L. Daulton and B. J. Little, "Determination of Chromium Valence Over the Range Cr(0)-Cr(VI) by Electron Energy Loss Spectroscopy," *Ultramicroscopy* 106 (2006): 561–573.

17. H. A. Wriedt, "The O–W (Oxygen–Tungsten) System," *Bulletin of Alloy Phase Diagrams* 10 (1989): 368–384.

18. R. L. Wagner, "Nitrogen Diffusion and Solubility in Tungsten," *Metallurgical Transactions* 1 (1970): 3365–3370.

19. C. Dupressoire, A. Rouaix-Vande Put, P. Emile, C. Archambeau-Mirguet, R. Peraldi, and D. Monceau, "Effect of Nitrogen on the Kinetics of Oxide Scale Growth and of Oxygen Dissolution in the Ti6242S Titanium-Based Alloy," *Oxidation of Metals* 87 (2017): 343–353.

20. C. Dupressoire, M. Descoins, A. Vande Put, et al., "The Role of Nitrogen in the Oxidation Behaviour of a Ti6242S Alloy: A Nanoscale Investigation by Atom Probe Tomography," *Acta Materialia* 216 (2021): 117134.

21. N. Zheng, W. J. Quadakkers, A. Gil, and H. Nickel, "Studies Concerning the Effect of Nitrogen on the Oxidation Behavior of TiAl-Based Intermetallics at 900°C," *Oxidation of Metals* 44 (1995): 477–499.

22. R. J. Hanrahan and D. P. Butt, "The Effects of Nitrogen on the Kinetics and Mechanisms of Oxidation of Titanium-Tantalum Alloys," *Oxidation of Metals* 48 (1997): 41–58.

23. N. J. Welch, M. J. Quintana, S. J. Kuhr, T. M. Butler, and P. C. Collins, "Intermediate and High-Temperature Oxidation Behavior of an Equiatomic TaTicr RCCA From 800°C to 1400°C," *International Journal of Refractory Metals and Hard Materials* 118 (2024): 106437.

24. N. J. Welch, M. J. Quintana, T. M. Butler, and P. C. Collins, "High-Temperature Oxidation Behavior of TaTiCr, Ta4Ti3Cr, and Ta4TiCr3 Concentrated Refractory Alloys," *Journal of Alloys and Compounds* 941, no. 29023 (2023): 169000.